photonics

MDPI

Communication

Preparation of Antireflection Microstructures on ZnSe Crystal by Femtosecond Burst Bessel Direct Laser Writing

Sikun Zhou, Junjie Yang, Sha Wang, Shutong Wang, Guoliang Deng * and Shouhuan Zhou

College of Electronics and Information Engineering, Sichuan University, Chengdu 610064, China
* Correspondence: gdeng@scu.edu.cn

Abstract: In this work, we fabricated the antireflection microstructures (ARMs) on ZnSe surfaces using a femtosecond Bessel direct laser writing in burst mode. The morphology and transmittance performance of ARMs with different single-pulse energies (from 200 nJ to 500 nJ), different burst modes (burst 1, 3, and 5 modes), different periods (from 3 µm to 6 µm), and different arrangements were investigated. The results revealed that tetragonally arranged ARMs fabricated by 500 nJ of single-pulse energy, the burst 3 mode, and a period of 3 µm show the best transmittance performance. The average transmittance of the ARMs was about 17.13% higher than that of bulk ZnSe in the range of 8–12 µm, and the highest transmittance of 81.75% (an improvement of 18.63% on one side of the ZnSe) was achieved at 12.36 µm. This process makes it possible to enhance ARMs' transmittance in the infrared wavelength range by using direct laser writing in burst mode.

Keywords: femtosecond laser; antireflection microstructure; burst mode; Bessel beam

check for updates

Citation: Zhou, S.; Yang, J.; Wang, S.; Wang, S.; Deng, G.; Zhou, S. Preparation of Antireflection Microstructures on ZnSe Crystal by Femtosecond Burst Bessel Direct Laser Writing. *Photonics* **2023**, *10*, 479. https://doi.org/10.3390/photonics10040479

Received: 24 March 2023
Revised: 17 April 2023
Accepted: 19 April 2023
Published: 21 April 2023

1. Introduction

Zinc selenide (ZnSe) is one of the most promising large bandgap semiconductors, which has aroused extensive attention because of its broad transparency in wavelengths (0.45–20 µm) [1], high refractive index (average n~2.45) [2], large bandgap (3.24 eV) [3], high exciton binding energy, and exciton gain. Due to the properties above, ZnSe was extensively used in optoelectronic devices [3–5] and infrared optics [6–10]. However, the high refractive index of infrared optics is a considerable challenge since it ultimately results in significant reflection losses (greater than 30%). Therefore, lowering the reflection losses brought on by the high refractive index is imperative. The conventional method to improve surface transmittance is plating a single or multi-layer antireflection coating (ARC) on the surface. This technique can provide more than 99% transmittance from visible to far-IR wavelengths, but the coating has poor chemical and mechanical durability. Fabricating an antireflection microstructure (ARM) on the surface is a different alternative method to increase surface transparency [11,12]. ARMs, which can significantly reduce Fresnel loss, can be prepared mainly by direct imprinting [13–15], dry or wet etching [16–21], laser-induced periodic surface structures [22–24], and direct laser ablation [25–33]. Among the conventional methods, the critical advantage of direct laser ablation is that the fabrication method is straightforward, and ARMs can be prepared on most materials.

Moreover, a few additional steps and materials are required during direct laser ablation, significantly reducing the production costs. Nowadays, many research groups have applied direct laser ablation to ZnSe [25,26], ZnS [27–31] and other materials [32,33] to fabricate ARMs. M.K. Tarabrin et al. reported the demonstration of ZnSe single crystal reflectivity reduction of up to 3% in a spectral range of 3.5 to 15 µm by using femtosecond laser pulses for microstructure formation without employing any etching technique [26]. Jia et al. fabricated micrometer-level inverted pyramid and cone arrays on ZnSe through femtosecond laser direct writing, and the measured transmittance was about 11.3% higher compared with that of plain ZnSe at 9 µm in an ideal situation [25]. When the period of the ARM is much smaller than the wavelength, the microstructure can be equivalent to a multilayer of the thin film medium. The periodicity, depth, and profile of the crater will greatly affect the equivalent refractive index gradient distribution. Based on the effective medium theory (EMT), a general rule is that the transmittance increases as the refractive index gradient becomes smoother. Hence, transmittance is determined by the morphological parameters of ARM [2]. Some articles have reported the influence of different shapes and craters on ARMs' performance [25,28], but a few papers have reported using femtosecond laser burst mode to prepare ARMs. In addition, laser burst mode operation can improve the ablation rates in semiconductors and dielectrics [34]. Therefore, exploring the effect of burst mode operation on crater depth and ARM performance is worthy of an in-depth study.

In this paper, we fabricated ARMs using an axicon-shaped femtosecond laser in burst mode on a single side of the ZnSe surface. Additionally, we examined the transmission of ARM in the infrared range of 8–12 μm using different burst modes, pulse energies, spatial periods, and arrangements of craters. The result illustrated that the increase in pulse energy and the number of sub-pulses could increase the depth of the crater and improve the performance of ARMs. The highest transmittance of 81.75% (improved by 18.63%) was achieved at 12.36 μm in the case of 500 nJ of single-pulse energy, the burst 3 mode, and a tetragonal arrangement. This process makes it possible to enhance ARMs' transmittance by using direct laser writing in burst mode.

2. Experiment

The laser source used to fabricate ARMs was a femtosecond fiber laser (Wuhan Yangtze Soton Laser Co., Ltd., Wuhan, China), with a center wavelength of 1030 nm and a pulse width of about 400 fs. It offers a horizontal, polarized, fundamental Gaussian mode, with a diameter of 3.9 mm. The repetition rate of 0.1 MHz was used in the experiment. The axicon (Edmund Inc.; base angle $\alpha = 2°$; refractive index $n_{\alpha x} = 1.45$) was used to convert the Gaussian beam to a Bessel beam. The 4f system, which consists of a plano-convex lens (f = 150 mm) and a micro-objective (100×, NA = 1.25, and a working distance of about 0.18 mm), was used to obtain suitable miniature Bessel beams, as is shown in Figure 1a. The ZnSe crystal (Optics & Fine Materials), with a diameter of about 10 mm and thickness of 1 mm, was mounted on a 3-axis motorized stage (P-611.3S, PI. Inc., Karlsruhe, Germany), with an accuracy greater than 10 nm. The shaped Bessel beam was then focused on the surface of ZnSe to fabricate ARMs.

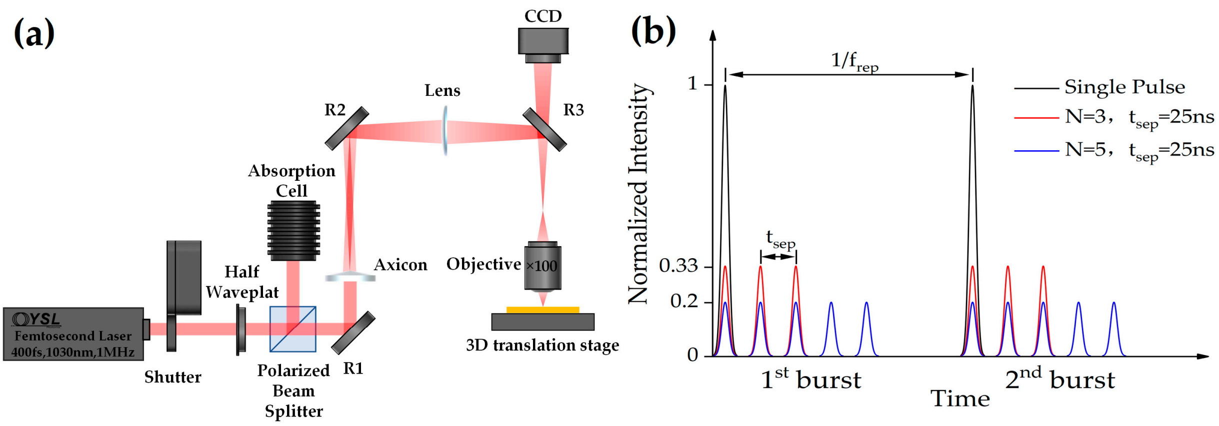

Figure 1. (**a**) Schematic diagram of femtosecond laser processing system. (**b**) A single laser pulse and two burst modes consisting of N = 3 and 5 pulses with tsep = 25 ns and the same total fluence; the frep represents the repetition of 0.1 MHz.

The single-pulse energy was set from 200 nJ to 500 nJ, with a time interval of 1 s. The time interval was determined by the time it took for the femtosecond laser to directly irradiate the ZnSe material. Pulse picker of the laser was performed to generate a pulse train with different numbers of sub-pulses (from 1 to 5; tsep = 25 ns) to prepare a single crater of ARM on the ZnSe sample, as illustrated in Figure 1b. The sub-pulses of the pulse train from 1 to 5 were defined as burst 1 to burst 5 modes, respectively. ARMs' structures of 0.1 × 0.1 mm^2 with a period from 3 μm to 6 μm were produced on the ZnSe surface. Finally, the scanning electron microscope (SEM, SU8220, Hitachi, Tokyo, Japan) was used to measure the ARMs' surface morphology. The profile of a single crater was examined using an atomic force microscope (AFM, Dimension ICON, Bruker, Billerica, MA, USA). Finally, transmission in the ranges from 5 μm to 15 μm was measured by a Fourier Transform Infrared Spectrometer (Nicolet Continuum FT-IR Microscope, Thermo Scientific, Waltham, MA, USA).

3. Results and Discussion

Several research groups have investigated ARMs and concluded that the structure depth is crucial for ARMs' performance [35,36]. The Bessel beam was used to increase the depth of the laser-induced crater and reduce the diameter of the crater. The calculated focused Bessel beam and Gaussian beam inside the ZnSe material are shown in Figure 2. As described in Figure 2a, the Bessel beam generated in the experiment contains a core surrounded by concentric higher-order rings, with most of the energy concentrated at the core of the Bessel beam. The energy accumulation of the Bessel beam along the axis of the propagation direction is depicted in Figure 2b, and the core shows a higher aspect ratio than that of the Gaussian beam. According to Figure 2b,c, the calculated Bessel beam FWHM values of the core along the radius and axis of the propagation direction were 688 nm and 6.02 μm, respectively. Compared to the calculated Bessel beam FWHM values of the core along the axis of the propagation direction, the Gaussian beam FWHM values of the core along the radius and axis of the propagation direction were 11.4 μm and ~0.8 μm, which is not conducive to the preparation of ARMs with deep craters, as is shown in Figure 2e,f. Thus, the Bessel beam was used to create deeper craters on ARMs, as well as improve the ARMs' performance.

To understand the influence of burst mode, single-pulse energy, structure period, and arrangement on ARMs' performance, ARMs of 0.1 × 0.1 mm^2 with various parameters of energy (E = 200 nJ, 300 nJ, 400 nJ, and 500 nJ), burst modes (burst 1, burst 3, and burst 5), and structure periods (p = 3 μm, 4 μm, 5 μm, and 6 μm) were prepared on the ZnSe sample. Figure 3a–d shows SEM images of different parameters of ARMs (E = 500 nJ; burst 3 mode; p = 3 μm, 4 μm, 5 μm, and 6 μm). The figure illustrates that the diameter of each crater is ~2 μm, and the craters generated severe recasting at the edge and the annular area.

The depth of craters with different single-pulse energies and burst modes are illustrated in Figure 4a. The AFM result demonstrates that single-pulse energy significantly impacts the depth of the craters, and the depth of the craters increases as the single-pulse energy level rises. Furthermore, compared to the traditional single-pulse operation, the burst mode operation has an essential influence on the depth of the craters. Among the burst mode operations, when the single-pulse energy level is lower (200 nJ) or higher (500 nJ), there is less difference in the craters' depth. When the energy of a single pulse is moderate (300–400 nJ), the depth of the craters grows as the number of sub-pulses rises. When the energy reaches 500 nJ, the number of sub-pulses rises, the craters' depth increases, and the depths of the craters are 1.09 μm (burst 1), 1.26 μm (burst 3), and 1.29 μm (burst 5), respectively. The profiles and the morphology of the craters with 500 nJ of single-pulse energy and in burst modes from burst 1 to burst 3 are shown in Figure 4b–g. In addition, the profiles around the center of the craters in burst 5 mode differ significantly from those in bursts 1 and 3 mode. By fitting the crater profiles, the profiles in burst 1 and burst 3 modes are more similar to the Gaussian type, while the profile in burst 5 mode is more similar to the Lorentz type. These two different shapes may impact the refractive index distribution at the interface between air and material, which might also influence the ARMs' performance [28].

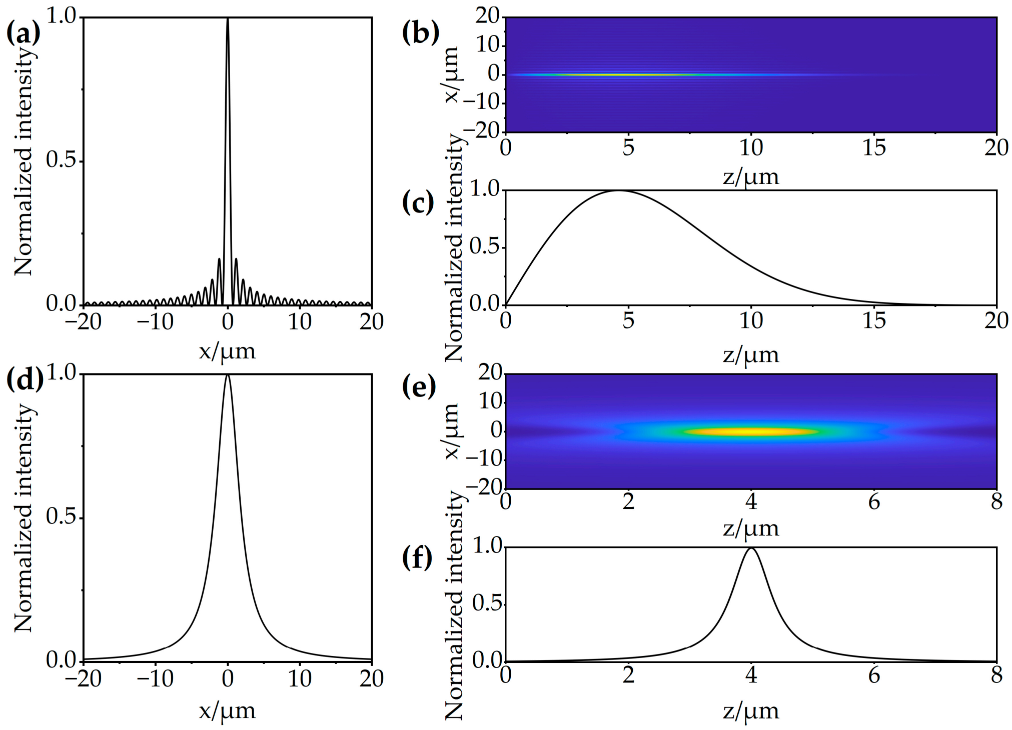

Figure 2. Normalized intensity distribution of the Bessel light field in the ZnSe material. (**a**) Radial light field cross-section at position y = 0. (**b**) Calculated Bessel beam intensity along propagation z. (**c**) The on-axis Bessel beam intensity along propagation z. Normalized intensity distribution of the Gaussian light field in the ZnSe. (**d**) Radial light field cross-section at position y = 0. (**e**) Calculated Gaussian beam intensity along propagation z. (**f**) The on-axis Gaussian beam intensity along propagation z.

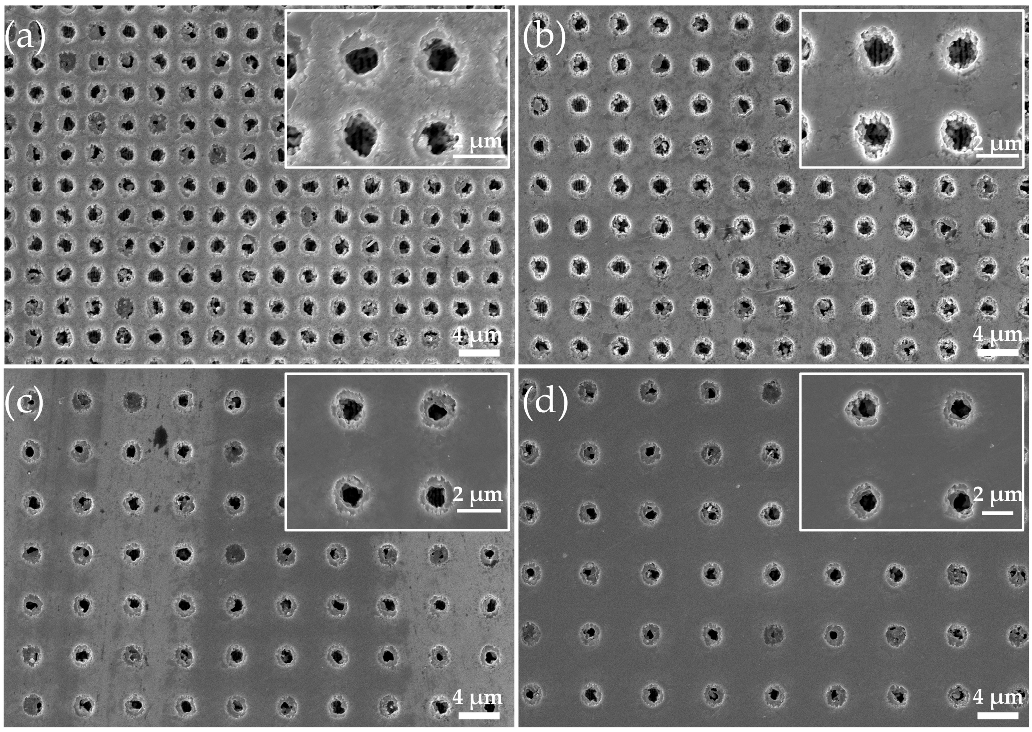

Figure 3. Different parameters of ARMs (E = 500 nJ; burst 3 mode; (**a**) p = 3 μm, (**b**) 4 μm, (**c**) 5 μm, and (**d**) 6 μm).

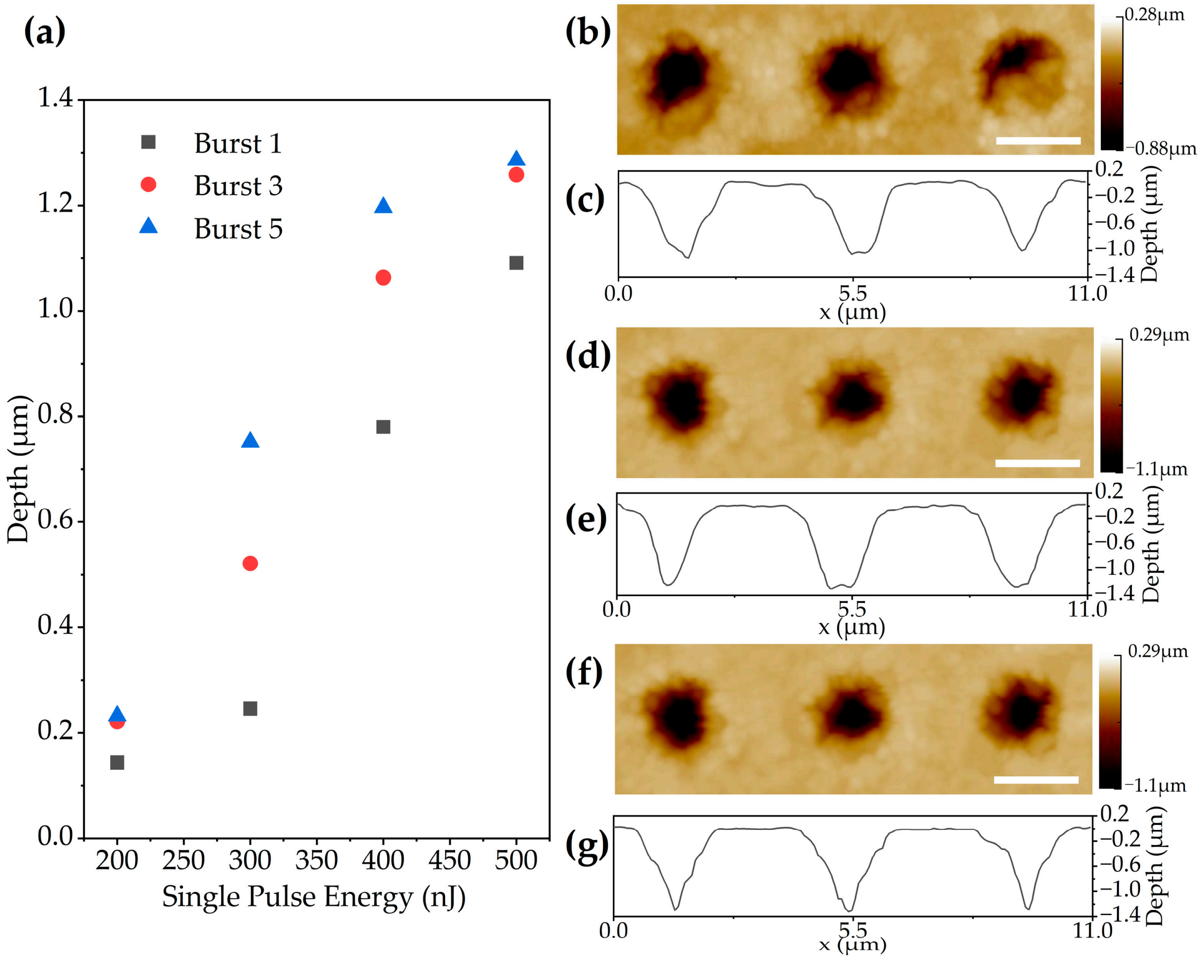

Figure 4. (**a**) The average depth of the ARMs' craters in different single-pulse energy and burst mode. The AFM image of ARMs' craters with 500 nJ of single-pulse energy and (**b**) burst 1, (**d**) burst 3, and (**f**) burst 5 modes. The profiles along the center of the ARMs' craters with 500 nJ of single-pulse energy and (**c**) burst 1, (**e**) burst 3, and (**g**) burst 5 modes. The white scale bar represents 2.5 μm.

Then, the transmission of the bulk ZnSe sample and ARMs of 0.1×0.1 mm^2 with various parameters was measured by using an FTIR spectrometer in the range of 5–15 μm. The results illustrated that the average transmission of the unprocessed bulk ZnSe sample was ~62.32% in the range of 5–15 μm. Based on the results of the craters' profiles, the number of sub-pulses and single-pulse energy have an impact on the depth and profile of the craters. To show the influence of craters' size and morphology on ARMs' performance, the transmission spectrums of ARMs at different single-pulse energies (E = 200 nJ, 300 nJ, 400 nJ, and 500 nJ) and the number of sub-pulses (burst 1, burst 3, and burst 5) were measured. From the transmission of different parameters shown in Figure 5a, compared to burst 1 and burst 5 modes, burst 3 mode exhibits higher transmittance values in the range of 8–15 μm. The average transmittance values of ARMs in the range of 8–15 μm are 79.45% (burst 3), 78.39% (burst 1), and 75.85% (burst 5), respectively. In addition, with the increase in single-pulse energy, there was a significant increase in transmittance, as illustrated in Figure 5b. The average transmittance values of ARMs at single-pulse energies from 200 nJ, 300 nJ, 400 nJ, to 500 nJ in the range of 8–15 μm were 67.66%, 72.00%, 76.55%, and 79.45%, respectively. This verifies that the depth of the ARM has an impact on the average transmittance. In the case of 500 nJ of single-pulse energy and burst 3 mode, the average transmittance of the ARM was improved by 17.13% in the range of 8–12 μm, and the highest transmittance of 81.75% (improved by 18.63%) was achieved at 12.36 μm.

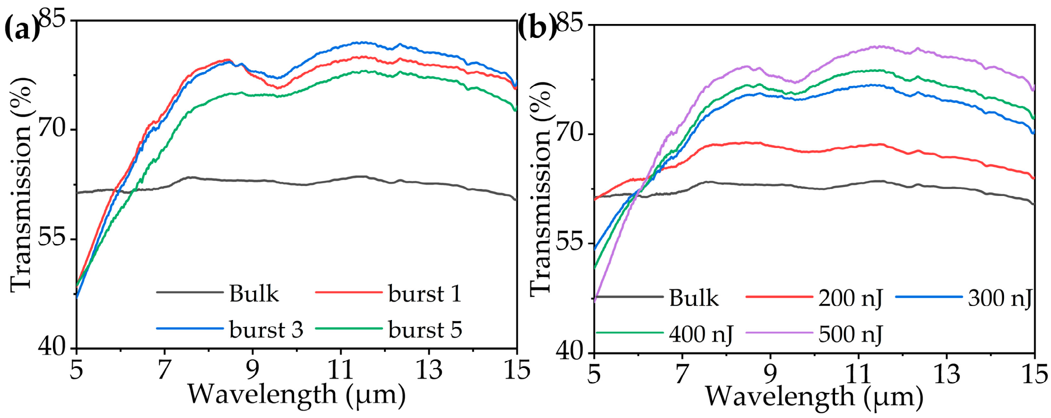

Figure 5. (**a**) Transmission of the ARMs in burst mode with the 500 nJ of single-pulse energy nJ in the range of 5–15 μm. (**b**) Transmission of the ARMs in burst 3 mode with the single-pulse energy from 200 nJ to 500 nJ in the range of 5–15 μm.

To compare the theoretical and experimental transmittance differences of the ARMs with 500 nJ of single-pulse energy and burst 1, burst 3, and burst 5 operations, the profiles along the center of the ARMs' craters were fitted, as depicted in Figure 6b,d,f. As previously illustrated in Figure 4c,e,g, the characteristics of the burst 1 and burst 3 modes are more similar to the Gaussian type, while burst 5 is similar to the Lorentz type. The general form of the Gaussian type is as follows:

$$y = y_0 + \frac{A}{w\sqrt{\frac{\pi}{4\ln 2}}} e^{\left(\frac{-4\ln 2(x-x_c)^2}{w^2}\right)} \tag{1}$$

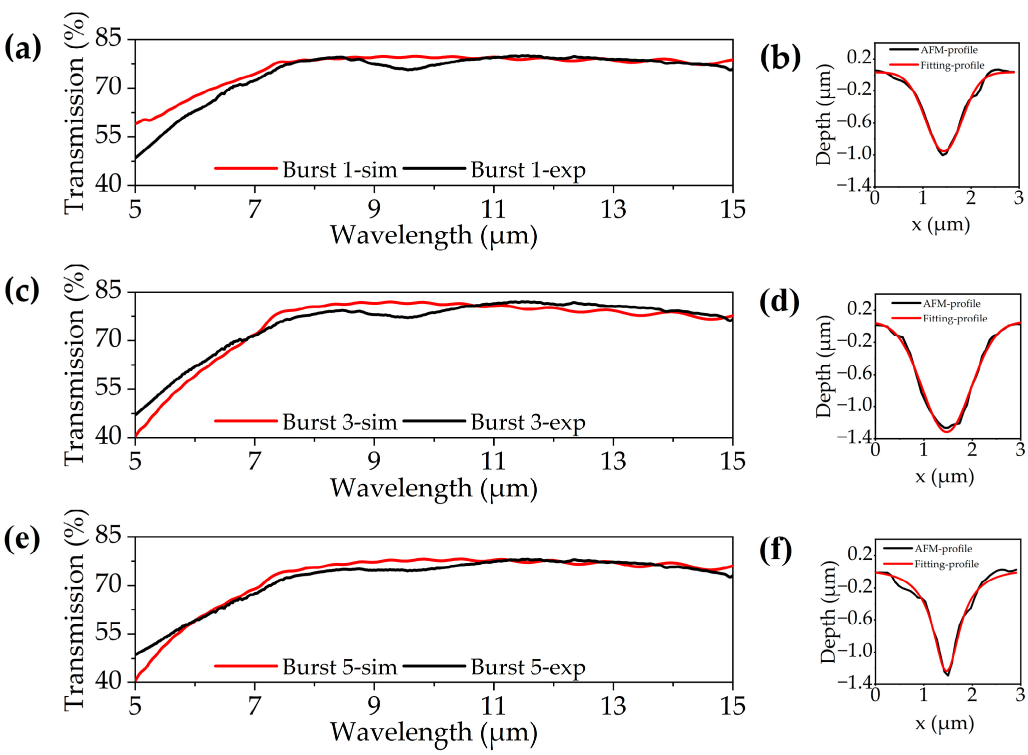

Figure 6. The simulation and experiment transmission of ARMs with 500 nJ of single-pulse energy in the range of 5–15 μm in (**a**) burst 1 mode, (**c**) burst 3 mode, and (**e**) burst 5 mode. The period of the ARMs was 3 μm. The fitting and experiment profile of the ARMs in (**b**) burst 1 mode, (**d**) burst 3 mode, and (**f**) burst 5 mode.

However, the Lorentz type is shown as:

$$y = y_0 + \frac{2A}{\pi}\left(\frac{w}{4(x - x_c)^2 + w^2}\right) \quad (2)$$

The parameters of the fitted profile of the ARMs' craters in three burst modes are shown in Table 1. Then, the Finite Difference Time Domain (FDTD) method was performed to analyze the ARMs' structure, which had the above-mentioned shape, in the range of 5–15 μm, as shown in Figure 6a,c,e, respectively. To ensure the accuracy of simulation calculations, we directly imported the three above-mentioned types of crater profiles into the theoretical calculations. The depths of the craters were 1.09 μm (burst 1), 1.26 μm (burst 3), and 1.29 μm (burst 5), respectively, and the diameter of each crater was ~2 μm. The period of the ARMs was set to 3 μm. The figure illustrates that the simulation and experiment results were in general agreement.

Table 1. The parameters of the fitted profile of the ARMs' craters in three burst modes.

	y_0 (μm)	A (μm)	w (μm)	x_c (μm)
Burst 1	0.0348	−0.93588	0.89048	1.43323
Burst 3	0.05236	−1.7127	1.17805	1.47026
Burst 5	0.05726	−1.37681	0.67921	1.46701

To further explore the effects of period and arrangement on ARMs' performance, ARMs with a period from 3 μm to 6 μm and hexagonal and tetragonal structures were fabricated in burst 3 mode with 500 nJ of single-pulse energy. As illustrated in Figure 7a, as the period of ARMs decreases, the transmission generally increases, and ARMs with the period of 3 μm exhibited a better performance. In the case of the ARMs with a period of 3 μm to 6 μm and with 500 nJ of single-pulse energy and a tetragonal arrangement, the average transmission values of the ARMs were 79.45%, 70.41%, 65.64%, and 64.06%, respectively. Similar to the tetragonal arrangement, the average transmission values of ARMs with the period of 3 μm to 6 μm in 500 nJ of single-pulse energy and hexagonal arrangement were 76.14%, 71.27%, 66.76%, and 64.68%, respectively, as is shown in Figure 7b. Compared to tetragonally arranged ARMs with the same parameters, the hexagonal arrangement ARM exhibited a better average transmission value with a period of 4 μm to 6 μm in the range of 8–15 μm, but exhibited a worse average transmission value with a period of 3 μm in the range of 8–15 μm.

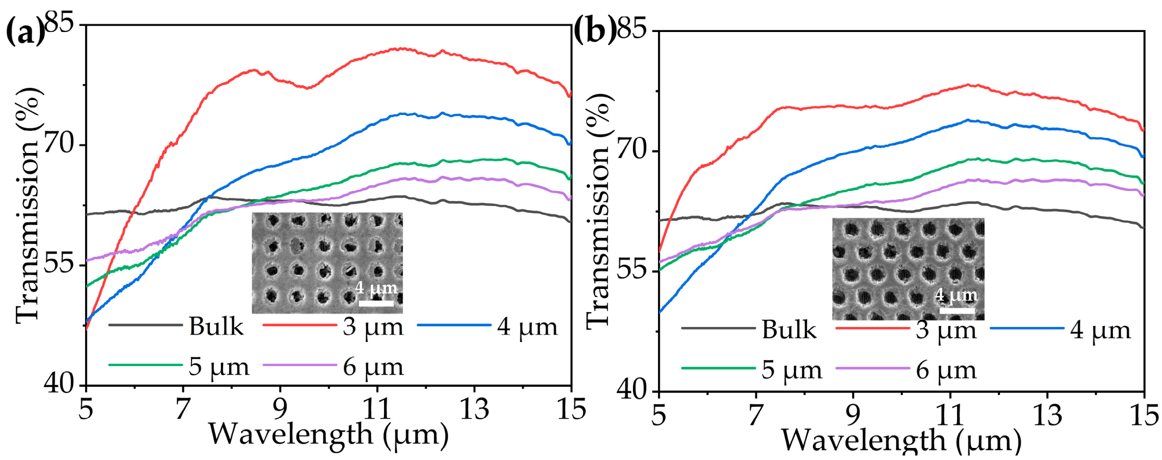

Figure 7. Transmission of the (**a**) tetragonal and (**b**) hexagonal arrangement ARMs with the period from 3 μm to 6 μm in the range of 5–15 μm (burst 3 mode; 500 nJ of single-pulse energy). The inset of the figure represents an SEM image of the arrangement of ARMs with a period of 4 μm.

4. Conclusions

In summary, we fabricated ARMs on the ZnSe surface using femtosecond Bessel direct laser writing in burst mode. The morphology and transmittance performance of ARMs with different single-pulse energies (from 200 nJ to 500 nJ), different burst modes (burst 1, burst 3, and burst 5), different structure periods (from 3 μm to 6 μm), and different arrangements were investigated. Among these parameters, the single-pulse energy and burst mode significantly impacted the depth of the ARMs' craters, and thus, affected the ARMs' performance. Then, the profiles of ARMs' craters (500 nJ of single-pulse energy) in three burst modes were fitted, and the FDTD method was performed to verify the ARMs' transmittance. The results illustrated that in the infrared range of 8–15 μm, the transmittance performance increased as the single-pulse energy increased. As the number of bursts increases, the depth of the ARMs' craters increases (from 1.09 μm in burst 1 to 1.29 μm in burst 5 mode). However, the best transmittance performance of the ARMs was in burst 3 mode rather than burst 5 mode, which may be due to the different shape of the ARMs' craters under other bursts. Finally, the average transmittance of the tetragonally arranged ARM was increased by 17.13% in the range of 8–12 μm, and the outstanding transmittance of 81.75% (improved by 18.63%) was attained in 12.36 μm for 500 nJ of single-pulse energy, the burst 3 mode, and the period of 3 μm. This process makes it possible to enhance ARMs' transmittance in the infrared range by using direct laser writing in burst mode.

Author Contributions: Conceptualization, methodology, software, investigation and writing original draft, S.Z. (Sikun Zhou); validation, resources, data curation, supervision, S.W. (Shutong Wang); formal analysis, data curation, J.Y.; validation, S.W. (Sha Wang); investigation, supervision, G.D.; supervision, validation, S.Z. (Shouhuan Zhou); All authors have read and agreed to the published version of the manuscript.

Funding: National Natural Science Foundation of China (61905168, 61905169, 61975137); Sichuan Province Science and Technology Support Program (No. 2022YFG0361).

Institutional Review Board Statement: Not applicable.

Informed Consent Statement: Not applicable.

Data Availability Statement: Not applicable.

Acknowledgments: We thank the National Natural Science Foundation of China and Sichuan Province Science and Technology Support Program for helping to identify collaborators for this work.

Conflicts of Interest: The authors declare no conflict of interest.

References

1. Harris, D.C. Durable 3–5 μm transmitting infrared window materials. *Infrared Phys. Technol.* **1998**, *39*, 185–201. [CrossRef]
2. Bushunov, A.A.; Tarabrin, M.K.; Lazarev, V.A. Review of Surface Modification Technologies for Mid-Infrared Antireflection Microstructures Fabrication. *Laser Photonics Rev.* **2021**, *15*, 2000202. [CrossRef]
3. Zhang, Y.; Wei, J.; Liu, T.; Zhong, Z.; Luo, Z.; Xiao, W.; Lv, B.; Zhou, X.; Liu, X. Tunable properties of ZnSe/graphene heterostructure as a promising candidate for photo/electro-catalyst applications. *Appl. Surf. Sci.* **2022**, *574*, 151679. [CrossRef]
4. Gao, M.; Yang, H.; Shen, H.; Zeng, Z.; Fan, F.; Tang, B.; Min, J.; Zhang, Y.; Hua, Q.; Li, L.S.; et al. Bulk-like ZnSe Quantum Dots Enabling Efficient Ultranarrow Blue Light-Emitting Diodes. *Nano Lett.* **2021**, *21*, 7252–7260. [CrossRef]
5. Wisniewski, D.; Byrne, K.; de Souza, C.F.; Fernandes, C.; Ruda, H.E. Enhancement of transport properties in single ZnSe nanowire field-effect transistors. *Nanotechnology* **2019**, *30*, 054007. [CrossRef] [PubMed]
6. Frolov, M.P.; Korostelin, Y.V.; Kozlovsky, V.I.; Podmar'kov, Y.P.; Skasyrsky, Y.K. High-energy thermoelectrically cooled Fe:ZnSe laser tunable over 3.75–4.82 mum. *Opt. Lett.* **2018**, *43*, 623–626. [CrossRef] [PubMed]
7. Pushkin, A.V.; Migal, E.A.; Tokita, S.; Korostelin, Y.V.; Potemkin, F.V. Femtosecond graphene mode-locked Fe:ZnSe laser at 4.4 microm. *Opt. Lett.* **2020**, *45*, 738–741. [CrossRef] [PubMed]
8. Pushkin, A.V.; Migal, E.A.; Uehara, H.; Goya, K.; Tokita, S.; Frolov, M.P.; Korostelin, Y.V.; Kozlovsky, V.I.; Skasyrsky, Y.K.; Potemkin, F.V. Compact, highly efficient, 2.1-W continuous-wave mid-infrared Fe:ZnSe coherent source, pumped by an Er:ZBLAN fiber laser. *Opt. Lett.* **2018**, *43*, 5941–5944. [CrossRef] [PubMed]
9. Zhang, F.; Yang, Q.; Bian, H.; Liu, F.; Li, M.; Hou, X.; Chen, F. Fabrication of ZnSe Microlens Array for a Wide Infrared Spectral Region. *IEEE Photonics Technol. Lett.* **2020**, *32*, 1327–1330. [CrossRef]

10. Devendra, K.C.; Shah, D.K.; Shrivastava, A. Computational study on the performance of zinc selenide as window layer for efficient GaAs solar cell. *Mater. Today Proc.* **2022**, *49*, 2580–2583. [CrossRef]
11. Pan, Y.; Hang, L.; Wu, Z.; Yin, Y. Design and fabrication of ultra broadband infrared antireflection hard coatings on ZnSe in the range from 2 to 16μm. *Infrared Phys. Technol.* **2009**, *52*, 193–195. [CrossRef]
12. Phillips, R.R.; Haynes, V.; Naylor, D.A.; Ade, P. Simple method for antireflection coating ZnSe in the 20 μm wavelength range. *Appl. Opt.* **2008**, *47*, 870–873. [CrossRef] [PubMed]
13. Lotz, M.R.; Petersen, C.R.; Markos, C.; Bang, O.; Jakobsen, M.H.; Taboryski, R. Direct nanoimprinting of moth-eye structures in chalcogenide glass for broadband antireflection in the mid-infrared. *Optica* **2018**, *5*, 557–563. [CrossRef]
14. Chenard, F.; Alvarez, O.; Buff, A. Mid-infrared chalcogenide fiber devices for medical applications. In Proceedings of the Optical Fibers and Sensors for Medical Diagnostics and Treatment Applications XVIII, San Francisco, CA, USA, 27 January–1 February 2018; pp. 104–112.
15. Sanghera, J.; Florea, C.; Busse, L.; Shaw, B.; Miklos, F.; Aggarwal, I. Reduced Fresnel losses in chalcogenide fibers by using anti-reflective surface structures on fiber end faces. *Opt. Express* **2010**, *18*, 26760–26768. [CrossRef]
16. Sun, H.; Liu, J.; Zhou, C.; Yang, W.; Liu, H.; Zhang, X.; Li, Z.; Zhang, B.; Jie, W.; Xu, Y. Enhanced Transmission from Visible to Terahertz in ZnTe Crystals with Scalable Subwavelength Structures. *ACS Appl. Mater. Interfaces* **2021**, *13*, 16997–17005. [CrossRef]
17. Zhang, Y.; Hu, X.; Wang, S.W.; Zhang, B.; Shi, L.; Liu, X.; Zi, J.; Lu, W. High transparent mid-infrared silicon "window" decorated with amorphous photonic structures fabricated by facile phase separation. *Opt. Express* **2018**, *26*, 18734–18748. [CrossRef]
18. Ye, X.; Shao, T.; Sun, L.; Wu, J.; Wang, F.; He, J.; Jiang, X.; Wu, W.D.; Zheng, W. Plasma-Induced, Self-Masking, One-Step Approach to an Ultrabroadband Antireflective and Superhydrophilic Subwavelength Nanostructured Fused Silica Surface. *ACS Appl. Mater. Interfaces* **2018**, *10*, 13851–13859. [CrossRef] [PubMed]
19. Lora Gonzalez, F.; Chan, L.; Berry, A.; Morse, D.E.; Gordon, M.J. Simple colloidal lithography method to fabricate large-area moth-eye antireflective structures on Si, Ge, and GaAs for IR applications. *J. Vac. Sci. Technol. B Nanotechnol. Microelectron. Mater. Process. Meas. Phenom.* **2014**, *32*, 051213. [CrossRef]
20. Malekmohammad, F.; Malekmohammad, M. Fabrication of a broadband anti-reflection layer using metal-assisted chemical etching. *Appl. Opt.* **2019**, *58*, 9039–9043. [CrossRef]
21. Lu, Y.T.; Barron, A.R. Nanopore-type black silicon anti-reflection layers fabricated by a one-step silver-assisted chemical etching. *Phys. Chem. Chem. Phys.* **2013**, *15*, 9862–9870. [CrossRef]
22. Granados, E.; Martinez-Calderon, M.; Gomez, M.; Rodriguez, A.; Olaizola, S.M. Photonic structures in diamond based on femtosecond UV laser induced periodic surface structuring (LIPSS). *Opt. Express* **2017**, *25*, 15330–15335. [CrossRef]
23. Ionin, A.A.; Klimachev, Y.M.; Kozlov, A.Y.; Kudryashov, S.I.; Ligachev, A.E.; Makarov, S.V.; Seleznev, L.V.; Sinitsyn, D.V.; Rudenko, A.A.; Khmelnitsky, R.A. Direct femtosecond laser fabrication of antireflective layer on GaAs surface. *Appl. Phys. B* **2013**, *111*, 419–423. [CrossRef]
24. Vorobyev, A.; Guo, C. Antireflection effect of femtosecond laser-induced periodic surface structures on silicon. *Opt. Express* **2011**, *19*, A1031–A1036. [CrossRef] [PubMed]
25. Cao, J.J.; Li, Q.K.; Yu, Y.H.; Yu, Y.S. Antireflection Microstructured Surface on ZnSe for Mid-infrared Spectral Region. *J. Laser Micro/Nanoeng.* **2019**, *14*, 120–123. [CrossRef]
26. Tarabrin, M.K.; Bushunov, A.A.; Lazarev, V.A.; Karasik, V.E.; Kozlovskiy, V.I.; Sviridov, D.E.; Korostelin, Y.V.; Frolov, M.P.; Skasyrsky, Y.K. Fabrication of anti-reflection microstructures on ZnSe single crystal by using femtosecond laser pulses. In Proceedings of the Laser Science, Washington, DC, USA, 18–21 September 2017; p. JTu2A.20.
27. Wang, L.; Xu, B.-B.; Chen, Q.-D.; Ma, Z.-C.; Zhang, R.; Liu, Q.-X.; Sun, H.-B. Maskless laser tailoring of conical pillar arrays for antireflective biomimetic surfaces. *Opt. Lett.* **2011**, *36*, 3305–3307. [CrossRef]
28. Zhang, F.; Wang, H.; Wang, C.; Zhao, Y.; Duan, J.A. Direct femtosecond laser writing of inverted array for broadband antireflection in the far-infrared. *Opt. Lasers Eng.* **2020**, *129*, 106062. [CrossRef]
29. Zhang, F.; Duan, J.; Zhou, X.; Wang, C. Broadband and wide-angle antireflective subwavelength microstructures on zinc sulfide fabricated by femtosecond laser parallel multi-beam. *Opt. Express* **2018**, *26*, 34016–34030. [CrossRef] [PubMed]
30. Wang, H.; Zhang, F.; Duan, J. Subwavelength Quasi-Periodic Array for Infrared Antireflection. *Nanomaterials* **2022**, *12*, 3520. [CrossRef] [PubMed]
31. Szliszka, E.; Czuba, Z.P.; Domino, M.; Mazur, B.; Zydowicz, G.; Krol, W. Ethanolic extract of propolis (EEP) enhances the apoptosis- inducing potential of TRAIL in cancer cells. *Molecules* **2009**, *14*, 738–754. [CrossRef]
32. Matsumura, T.; Young, K.; Wen, Q.; Hanany, S.; Ishino, H.; Inoue, Y.; Hazumi, M.; Koch, J.; Suttman, O.; Schutz, V. Millimeter-wave broadband antireflection coatings using laser ablation of subwavelength structures. *Appl. Opt.* **2016**, *55*, 3502–3509. [CrossRef] [PubMed]
33. Bushunov, A.A.; Tarabrin, M.K.; Lazarev, V.A.; Karasik, V.E.; Korostelin, Y.V.; Frolov, M.P.; Skasyrsky, Y.K.; Kozlovsky, V.I. Fabrication of anti-reflective microstructures on chalcogenide crystals by femtosecond laser ablation. *Opt. Mater. Express* **2019**, *9*, 1689–1697. [CrossRef]
34. Hodgson, N.; Allegre, H.; Starodoumov, A.; Bettencourt, S. Femtosecond Laser Ablation in Burst Mode as a Function of Pulse Fluence and Intra-Burst Repetition Rate. *J. Laser Micro Nanoeng.* **2020**, *15*, 236–244. [CrossRef]

35. Deinega, A.; Valuev, I.; Potapkin, B.; Lozovik, Y. Minimizing light reflection from dielectric textured surfaces. *JOSA A* **2011**, *28*, 770–777. [CrossRef] [PubMed]
36. Boden, S.A.; Bagnall, D.M. Tunable reflection minima of nanostructured antireflective surfaces. *Appl. Phys. Lett.* **2008**, *93*, 133108. [CrossRef]